Attosecond pulse shaping using partial phase matching

Attosecond pulse shaping using partial phase matching

Dane R Austin[1,3] **and Jens Biegert**[1,2]

[1] ICFO-Institut de Ciences Fotoniques, Castelldefels E-08860 Barcelona, Spain
[2] ICREA-Institució Catalana de Recerca i Estudis Avançats, E-08010 Barcelona, Spain
E-mail: d.austin@ic.ac.uk

Abstract

We propose a method for programmable shaping of the amplitude and phase of the extreme ultraviolet and x-ray attosecond pulses produced by high-order harmonic generation. It overcomes the bandwidth limitations of existing spectral filters and enables removal of the intrinsic attosecond chirp as well as the synthesis of pulse sequences. It is based on partial phase matching using a longitudinally addressable modulation. Although the method is in principle applicable to any form of partial phase matching, we focus on quasi-phase matching using a counterpropagating pulse train. We present simulations of the production of isolated attosecond pulses at 250 eV, including a 31 as transform-limited pulse, tunably chirped pulses and double pulses.

S Online supplementary data available from stacks.iop.org/njp/16/113011/mmedia

Keywords: attosecond pulses, ultrafast optics, pulse shaping, high-order harmonic generation

---

[3] Current address: Imperial College London, London SW7 2AZ, UK.

1. Introduction

Coherent extreme ultraviolet (XUV) and soft x-ray radiation, produced by high-order harmonic generation (HHG) in an intense laser field, is central to attoscience [1, 2]. Spectra spanning 200–1600 eV, with the potential to support temporal features of 2.5 as duration, have been generated, providing the raw material for coherent excitation of atomic scale electron dynamics down to the inner shell. At present, there is no general means of controlling the spectral and temporal profile of radiation produced via HHG on the attosecond timescale. Bandpass and dispersive filtering, the latter being necessary to eliminate the attosecond chirp that is intrinsic to HHG, have been demonstrated using metal films, gases, and multilayer mirrors, but these lack continuous tunability and have only been demonstrated below 150 eV for bandwidths of ≈ 50 eV [3–5].

The ability to arbitrarily shape HHG over its entire bandwidth would improve existing experiments and enable others, analogous to the role of dispersion control [6] and pulse shaping [7] in femtosecond science and technology. Using harmonic spectra from standard IR sources, pulses as short at 2.5 as could be generated [8]. Current XUV-pump IR-probe studies of single-photon ionization [9, 10] could be performed over a range of photon energies, accessing a wider range of initial states and potentially disentangling the roles of the Coulomb potential and the IR probe. Coherently controlled wavepackets [11] could be launched and probed. With sufficient intensity, XUV-pump XUV-probe [12] spectroscopy and coherent control [13] could be achieved.

Macroscopic effects—the coherent sum of the dipole response of all the target atoms—play a crucial role in attosecond pulse generation via HHG [14]. Of primary importance is the wave vector mismatch Δk between the laser-driven dipole excitation and the propagating harmonics. Whilst the latter propagate very close to c, the former is influenced by diffraction in the focus or waveguide, dispersion of the neutral gas and free-electron plasma, and the intensity dependence of the electron in the continuum. Partial phase matching [15, 16], achieved with a longitudinal modulation of the dipole excitation with wavevector $K = \Delta k$, can be used to overcome a phase mismatch. Various methods have been demonstrated or proposed for achieving the longitudinal modulation including a corrugated waveguide [17, 18], multi-mode beating [19], modulation of the target gas density [20], a counterpropagating pulse train (CPT) [16, 21, 22], or a counterpropagating pulse [23]. Regardless of the particular implementation, partial phase matching is inherently dependent on the harmonic frequency and hence offers a degree of control over the spectrum. Here, we show using theory and numerics that using partial phase matching with a longitudinally addressable modulation, one may not only compensate the attosecond chirp, but also synthesize an arbitrary *in situ* amplitude and phase filter for HHG, opening the door to pulse shaping in the XUV and soft x-ray regions. The method is applicable over the whole spectrum up to kiloelectron-volt photon energies. The type of partial phase matching we consider is quasi-phase matching (QPM) with a CPT [16, 21, 22], since this is in principle fully programmable using femtosecond pulse shaping [7].

The remainder of this paper is structured as follows: we give a conceptual description of the method in section 2.1, and then a detailed derivation in section 2.2. We present our numerical model in section 2.3 and then in section 2.4 give a procedure for designing a CPT to obtain a specified attosecond pulse. We then present several examples of controlling isolated attosecond pulse production: a transform limited pulse (section 3.1), pulses with a specified spectral phase (section 3.2), and arbitrarily shaped pulses (section 3.3). We then consider the

impact of some realistic experimental imperfections (section 3.4) and discuss the applicability of the idea to a many-cycle drive pulse (section 3.5). Section 4 concludes.

2. Methods

2.1. Concept

The essence of our method is that in HHG, a phase velocity mismatch is almost always accompanied by a group velocity mismatch i.e. $\Delta k(\omega) = \Delta n \omega / c$, where $\Delta n = n(\omega_1) - n(\omega)$ is the difference between the refractive indices at the fundamental frequency ω_1 and the harmonics ω. This is because in HHG, the group delay of the constituent attosecond bursts is dictated by the laser field oscillations (rather than their envelope as with perturbative harmonic generation). The phase velocity of the laser is therefore imparted on the group velocity of the dipole response. Partial phase matching with wavenumber K occurs at a single frequency $\omega = Kc/\Delta n$. If K varies along the propagation axis, then multiple frequencies are phase matched, but because of the group-velocity mismatch, their group delays will differ, producing a relative chirp between the dipole excitation and the macroscopically generated field. A linear variation $K_1 = dK/dz$ leads to a quadratic spectral phase $\Delta\phi_2$ given by

$$\Delta\phi_2 = \left(\frac{\Delta n}{c}\right)^2 \frac{1}{K_1}, \tag{1}$$

tunable in both magnitude and sign through K_1. As we will show, this effect can compensate the attosecond chirp leading to transform limited pulses, or be generalized to enable arbitrary pulse shaping.

Figure 1 is a cartoon illustration of the concept, depicting compensation of the positive chirp of the short trajectories assuming a subluminal laser phase velocity i.e. $n(\omega_1) > 1$. For simplicity, and a reasonable approximation in most cases, we assume $n(\omega) = 1$ for the harmonics. At two points z_1 and z_2 along the propagation axis z, the laser field E (red) and the kinetic energy (KE) (green) of the recombining electron are plotted versus time in the retarded frame

$$t = \bar{t} - z/c, \tag{2}$$

where $\bar{t}$ is time in the lab frame. The laser field, the electron motion that it drives, and the resulting time–frequency structure of the high-harmonic emission, are delayed by an amount $(n(\omega_1) - 1)z/c$ upon propagation. This is shown by the sloped gray lines through the laser field peaks (red dots) and classical cutoffs (green dots). A negatively chirped modulation is applied (blue) to achieve partial phase matching. For the purpose of this explanation, the physical mechanism of the modulation is unimportant. The key point is that the harmonic frequency which is partially phase matched, indicated by the horizontal dashed lines, decreases with z. The chirp rate of the modulation is chosen using (1) such that the recombination time of the partially phase matched harmonics from the short trajectory is constant with z, indicated by the vertical dashed line. Therefore, the macroscopic emission from the short trajectory is unchirped (whereas the macroscopic emission from the long trajectory has additional chirp). This is depicted in the gray box.
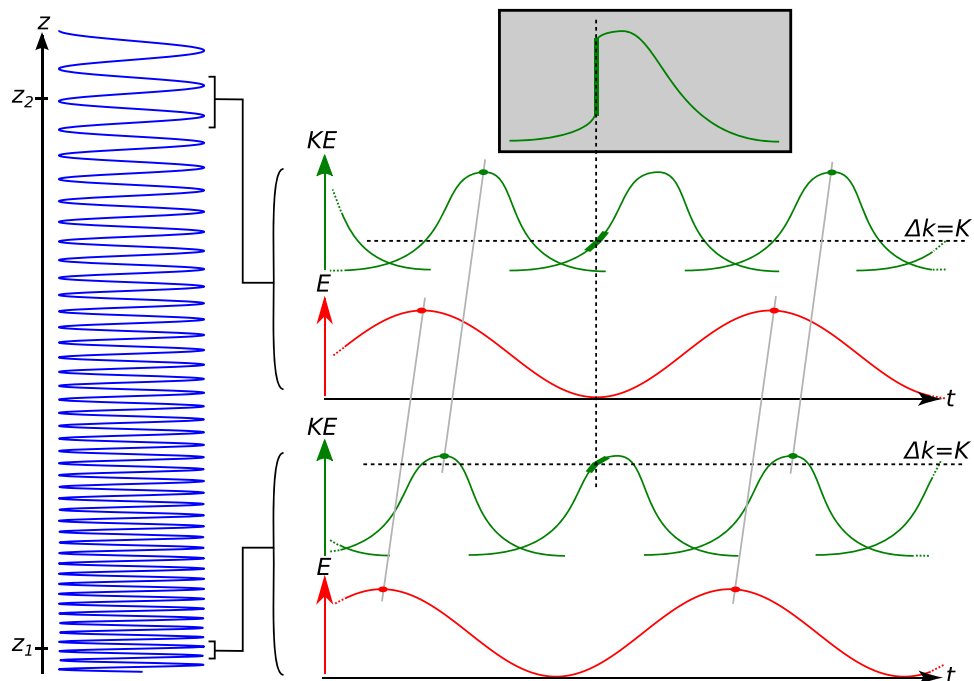
Figure 1. Attosecond chirp removal through negatively chirped partial phase matching; longitudinal modulation (blue), laser field E (red) and electron kinetic energy KE (green) versus retarded time t, frequency of partial phase matching (horizontal dashed lines), and recombination time of partially phase matched harmonics (vertical dashed line). The gray box shows the time-frequency structure of the macroscopic emission.

2.2. Derivation

We now present a more detailed derivation of the above idea, making use of the quantum path picture of HHG [24]. The macroscopic harmonic field $E(\omega)$ is expressed as

$$E(\omega) = \sum_n \int dz D_n(\omega, z). \tag{3}$$

Here, n labels quantum paths, $D_n(\omega, z)$ is the contribution at transverse slice z incorporating the single-atom response (which itself incorporates all propagation effects of the fundamental), the local target density, propagation of the harmonics to the end of the medium, any spatial or spectral filters, and the modulation used to induce partial phase matching. We focus on a single quantum path which we assume to dominate the macroscopic field, at least in the spectral region of interest, and therefore will drop the subscripts for clarity. If this and another path coalesce (such as when the laser intensity drops below the point at which the classical cutoff equals ω) then the contribution of the other path can in principle be included with the uniform approximation.

  We assume that, for every frequency ω of interest, there is exactly one point $z_s(\omega)$ at which partial phase matching occurs i.e. at which the phase $\phi_D(\omega, z)$ of $D(\omega, z)$ is stationary. We apply a second-order stationary phase approximation to (3):

$$E(\omega) \approx \left(\frac{1}{2\pi} \frac{\partial^2 \phi_D(\omega, z_s)}{\partial z^2} \right)^{-\frac{1}{2}} \left| D(\omega, z_s) \right| \mathrm{e}^{\mathrm{i}\phi_D(\omega, z_s(\omega)) + \mathrm{i}\frac{\pi}{4}}. \tag{4}$$

Put abstractly, our method consists of manipulating $z_s(\omega)$ so as to achieve a desired macroscopic spectral phase $\phi_E(\omega) = \phi_D(\omega, z_s(\omega)) + \pi/4$. For clarity, we drop explicit ω and z dependence (this is included in all numerics). We now explicitly incorporate partial phase matching by writing $\phi_D = \phi_d - \Phi$ where ϕ_d is the phase without partial phase matching, and

$$\Phi(z) = \int_0^z K(z') \mathrm{d}z', \tag{5}$$

where K the wavenumber of the modulation induced to achieve partial phase matching. The partial derivatives of ϕ_d are the phase mismatch $\Delta k = \partial_z \phi_d$ and the group delay $\tau = \partial_\omega \phi_d$. To obtain a target group delay $\tau_E = \partial_\omega \phi_E$, we start from $(\omega_c, z = 0)$ and trace a contour $\omega_P(z)$ of $\tau - \tau_E$. Then, we ensure that this contour is also the line of stationary phase (i.e. $\omega_P(z)$ is the inverse function of $z_s(\omega)$) by setting

$$K(z) = \Delta k(\omega_P(z), z). \tag{6}$$

This procedure is used in subsequent sections of this paper to choose the wavenumber of the partial phase matching modulation. In an experiment, $\tau(\omega, z)$ and $\Delta k(\omega, z)$ could be obtained in a calibration step, with trial CPT sequences generated by a programmable femtosecond pulse shaper [7].

    While the global condition (6) is general and correct to all orders in ω and z, one may also obtain a local condition involving lowest-order partial derivatives. This is useful for a back-of-an-envelope calculation and formalizes the simpler argument leading to (1). Taylor expanding ϕ_D around a nominal centre frequency $\omega = \omega_c$, and without loss of generality choosing $z_s(\omega_c) = 0$ and the time origin such that $\tau(\omega = \omega_c, z = 0) = 0$, we have

$$\phi_D \approx \frac{\delta}{2} z^2 + \kappa z(\omega - \omega_c) + \frac{\gamma}{2}(\omega - \omega_c)^2, \tag{7}$$

where $\delta = \partial_{zz}^2 \phi_d - K_1$ is the linearly varying phase mismatch, $K_1 = \mathrm{d}K/\mathrm{d}z$, $\kappa = \partial_{z\omega}^2 \phi_d$ is the group delay mismatch, and $\gamma = \partial_{\omega\omega}^2 \phi_d$ is the intrinsic attosecond chirp which we wish to compensate. By definition of the stationary point $z_s(\omega)$,

$$\frac{\mathrm{d}z_s}{\mathrm{d}\omega} = -\frac{\kappa}{\delta}. \tag{8}$$

Substituting (8) into (7) gives

$$\frac{\mathrm{d}^2 \phi_E}{\mathrm{d}\omega^2} = \gamma - \frac{\kappa^2}{\delta}. \tag{9}$$

Equation (9) is a generalized restatement of (1) and compactly summarizes the method. It states that in addition to the intrinsic attosecond chirp γ, the macroscopic chirp has an additional component caused by the combination of a linearly varying partial phase matching condition δ and a group velocity mismatch κ. It has a simple graphical interpretation in terms of caustics. If the phase $\phi_D(\omega; z)$ is plotted versus ω for various values of z, then by the stationary phase condition the macroscopic spectral phase $\phi_E(\omega)$ is the locus of extreme values, or the caustic, of $\phi_D(\omega, z)$. (The $\pi/4$ offset introduced in (4) by the stationary phase approximation only affects
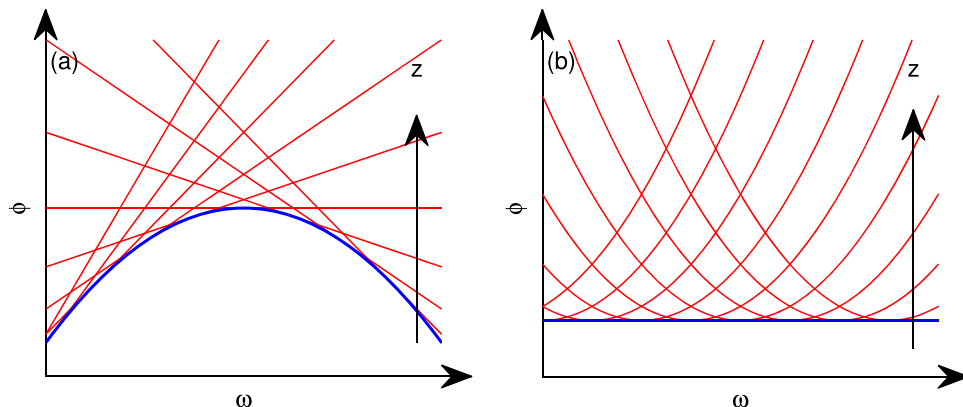
Figure 2. Caustics interpretation of attosecond chirp control; spectral phase of contributions from individual z slices (red) and their caustic (blue), the spectral phase of the macroscopic field. (a) Linearly varying phase mismatch $\delta > 0$, group delay mismatch $\kappa > 0$, attochirp $\gamma = 0$. (b) With δ, κ and γ satisfying the condition for zero net attochirp.

the absolute phase of the attosecond pulses.) Figure 2 illustrates this. In figure 2(a), the intrinsic attochirp $\gamma = 0$, but the interplay of the quadratically varying offset $\delta z^2/2$ and linearly varying slope $\kappa z(\omega - \omega_c)$ means that the caustic has a negative curvature. Figure 2(b) shows the case for $\delta\gamma = \kappa^2$, which gives a straight caustic and hence zero macroscopic attosecond chirp. Caustics were recently introduced to attoscience [25] for understanding and manipulating the single-atom response. In that work, the variable of integration—the *state variable* in the language of catastrophe theory [26], which describes caustics—was the ionization time, a parameter of the single-atom response. Here, the state variable is z, illustrating that caustics are useful in understanding the macroscopic as well as microscopic picture of HHG. In both cases, the harmonic frequency ω is the *control parameter*, on which the integral explicitly depends.

2.3. Numerics

In our numerical model, the drive laser propagates according to the forward Maxwell equation [27, 28] which includes full dispersion curves, paraxial diffraction, self-phase modulation, and Drude plasma-induced dephasing and absorption [29]. The model has three spatial dimensions with cylindrical symmetry. Ionization rates are calculated using the ADK formula [30]. Numerically, we integrate the equation using a preconditioned Runge–Kutta method, with adaptive step-sizing, in a manner similar to that used in solving the time dependent Schrödinger equation [31]. Dispersion and diffraction are applied in the frequency–wavenumber $(\omega, k_\perp)$ domain, whilst nonlinear effects are applied in the (t, r) domain. The discrete Fourier transform and the quasi-discrete Hankel transform [32] are used to switch between the two domains. Once the laser field has been calculated at all points in the interaction region, it is resampled to a finer space–time grid, and the microscopic HHG response computed at every point. We use an augmented strong-field approximation (SFA) model [33, 34], with an electron birth factor that incorporates the ADK ionization rate [35–37] and photorecombination cross section for the recombination step [38]. Specifically, the high-frequency part of the dipole acceleration is (in atomic units)

$$a(t) = \sum_n g(t_b) f(t_b) \left[\frac{2\pi i}{t - t_b} \right]^{3/2} g^*(t) d(v(t)) e^{iS}, \tag{10}$$

where n sums over different half-cycles of the drive pulse in which strong-field ionization occurs, t_b is the (real) electron birth time corresponding to recollision at t assuming a zero birth velocity, $g(t)$ is the ground state amplitude, $f(t)$ is the zero-transverse-momentum component of the continuum electron wavepacket (incorporating the instantaneous ionization rate) [36], $v(t)$ is the continuum electron velocity, $d(v)$ is the calculated photorecombination cross section [38] of a model helium atom, and S is the usual action integral. All quantities have spatial (r, z) dependence, but this is hidden for clarity.

The main novel aspect of our numerical model is its incorporation of the CPT, which is done as follows. The spatio-temporal field profile $E_C(t, r, z)$ is calculated from a specified initial condition at a reference plane using paraxial diffraction and dispersion. Nonlinear effects are ignored because the CPT peak intensity remains below $0.2\,\mathrm{TW\,cm^{-2}}$. Any interaction with the drive pulse is also ignored. The influence of the CPT on the single-atom response is approximated to a first-order perturbation to the SFA action integral [39, 40]. Specifically,

$$\Delta S = -\int_{t_b}^{t_r} v(t, t_b) A_C(t) dt, \tag{11}$$

where t_b and t_r are the SFA birth and return times, $v(t, t_b)$ is the velocity of a continuum electron born at t_b, and $A_C(t)$ is the vector potential of the CPT. The temporal envelope of the CPT varies much more slowly than that of the drive pulse. Therefore, for each single-atom calculation, we approximate the CPT by a sinusoid with amplitude, phase and frequency equal to that of the CPT at the peak $t_0(r, z)$ of the drive pulse envelope. The perturbation to the action can then be written as

$$\Delta S = |E_C| \, \alpha \cos\left(\phi_C + \beta\right), \tag{12}$$

where $|E_C|$, ϕ_C, and ω_C are the amplitude, phase and instantaneous frequency of the CPT sampled at (t_0, r, z) and α and β describe the sensitivity of the action to a sinusoidal perturbation, in polar form:

$$\alpha = \sqrt{\Delta S_I^2 + \Delta S_Q^2}, \tag{13}$$

$$\beta = \tan^{-1}\left(\Delta S_Q / \Delta S_I\right), \tag{14}$$

$$\Delta S_I = -\int_{t_b}^{t_r} v(t, t_b) \cos\left(\omega_C t\right), \tag{15}$$

$$\Delta S_Q = -\int_{t_b}^{t_r} v(t, t_b) \sin\left(\omega_C t\right). \tag{16}$$

Note that α depends on the drive pulse profile, the quantum trajectory in question, and ω_C. Because of the counterpropagation, the CPT phase varies longitudinally as $\phi_C \approx 4\pi z / \lambda_C$, much more rapidly than the longitudinal evolution of the drive pulse. Therefore, as in previous treatments [41] we average over rapid oscillations of the induced phase modulation so that the effect of the CPT is to modulate the amplitude of the single-atom response by a factor

$$G = \langle e^{i\Delta S} \rangle = J_0\big(\alpha \, |E_C|\big), \tag{17}$$

where $\langle \cdot \rangle$ denotes averaging and J_0 is the zeroth-order Bessel function. The factor G, with full dependence on the recombination time t, the half-cycle of electron birth n, and radial and longitudinal position (r, z), is applied to the dipole acceleration (10). The macroscopic field is then calculated by integrating over all (r, z) and summing over n, incorporating the local gas density, diffraction, and absorption and dispersion from the neutral species in the target. Each of the simulations presented below took approximately one hour on a desktop PC.

2.4. Design of CPT

Section 2.2 presented formalism for choosing the wavenumber $K(z)$ so as to achieve a desired attosecond chirp. We now apply this to the design of the CPT. We define the counter-propagating retarded time

$$t_C = \bar{t} + z/c. \tag{18}$$

Since the peak of the drive pulse occurs at $t \approx 0$, then via (2) and (18) the drive pulse overlaps with the CPT temporal envelope at $z = ct_C/2$. When the drive pulse is overlapped with one of the sub-pulses of the train, harmonic emission is suppressed via (17). To achieve a modulation with wavenumber K, one therefore requires that $|E_C(t_C)|$ be oscillatory with period $4\pi/(cK)$, thus determining the inter-pulse spacing.

Previous authors have considered the relative merits of different profiles for the pulses in the train [41]. Here, we choose

$$\left| E_C \left(\frac{2z}{c} \right) \right| = f[\Phi(z), \epsilon(z)]/\alpha\big(\omega_P(z), z\big), \tag{19}$$

where $\alpha(\omega_P, z)$ the frequency-dependent phase perturbation coefficient (13) and

$$f(\Phi, \epsilon) = J_0^{-1}[\epsilon(0.701 \cos \Phi + 0.299)], \tag{20}$$

chosen to map the full range of the zeroth order Bessel function in (17) onto a sinusoid of phase Φ and amplitude ϵ. This gives optimal QPM efficiency and minimizes unwanted spatial overtones. The parameter ϵ is used below to extend the method to amplitude modulation; for maximum diffraction efficiency we take $\epsilon = 1$. Equation (19) is evaluated at $r = 0$, which means that the diffraction efficiency is only optimal on axis and falls off radially. The transverse spatial dependence is fully included in our simulations. Note also that in our simulations, the coefficient α describing the sensitivity of the action to the counter-propagating field is calculated taking into account the temporal profile of the drive pulse using (11). However, for design purposes an excellent approximation is to treat each half cycle of the drive field as sinusoidal, parameterized only by its amplitude E_D and frequency ω_D. In this case, a scaling analysis of (11) gives

$$\alpha = \bar{\alpha}(\bar{\omega}, \omega_C/\omega_D) \frac{E_D}{\omega_D^3}, \tag{21}$$

where $\bar{\omega} = (\omega - I_p)/(4U_p)$ (I_p and U_p are the ionization pontential and ponderomotive potential, respectively) is frequency normalized to the cutoff i.e. $0 < \bar{\omega} < 3.17$ and $\bar{\alpha}(\bar{\omega}, \bar{\omega}_C)$ is calculated using (13) using a sinusoidal drive field of unit amplitude and frequency and a counter-propagating field of unit amplitude and frequency $\bar{\omega}_C$. Figure 3 presents $\bar{\alpha}$ for the short
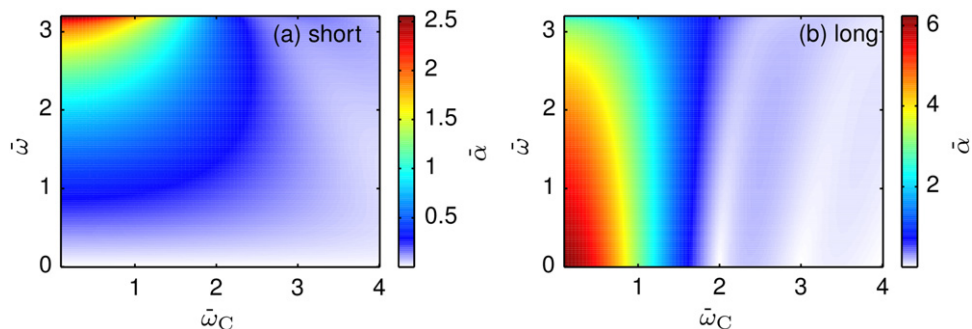
Figure 3. Normalized coefficient of phase perturbation $\bar{\alpha}$ of the (a) short and (b) long trajectories to a sinusoidal counterpropagating field versus normalized harmonic frequency $\bar{\omega}$ and the ratio $\bar{\omega}_C$ of the optical frequencies of the counterpropagating and drive fields.

and long trajectories. The ω_D^{-3} scaling of α will make achieving sufficient CPT intensity significantly easier at longer drive wavelengths.

A further generalization is to exploit the one-to-one correspondence between z and ω by directly modulating the phase and amplitude of the CPT, producing an arbitrary transfer function $H(\omega) = |H(\omega)| \exp [i \arg H(\omega)]$ with given amplitude $|H(\omega)|$ and phase $\arg H(\omega)$. In (19), one sets

$$\Phi(z) = \int K(z)\mathrm{d}z - \arg H\left(\omega_P(z)\right), \text{ and } \epsilon(z) = \left| H\left(\omega_P(z)\right)\right|, \tag{22}$$

where $K(z)$ is chosen using (6). In this sense, the method is analogous to acousto-optic programmable dispersive filters (AOPDFs) used for femtosecond pulse shaping [42]. In these devices, an incident pulse polarised along one axis of a birefringent crystal is scattered into the other axis by a density modulation caused by a programmable acoustic wave. The local period of the acoustic wave determines the frequency of the light scattered at a particular position along the propagation axis. In our proposed technique, the drive laser and the harmonics play the role of the incident and scattered field in the AOPDF respectively, whilst the refractive index difference between the optical and harmonic frequencies plays the role of the birefringence.

3. Results

3.1. Production of a transform-limited isolated attosecond pulse

Our first example is the production of a transform-limited isolated attosecond pulse. The driving laser pulse is temporally and spatially Gaussian with 9 fs full-width at half maximum (FWHM) duration, 1.8 μm centre wavelength, 220 μJ energy, and with carrier leading the envelope by 20°. These parameters are realistic due to recent advances in the generation of high-energy few-cycle infrared pulses [43–45]. It is focused to a e^{-2} radius of 50 μm a distance 1.4 mm before a jet of helium with peak pressure 5 bar and FWHM thickness 1.4 mm. The generated macroscopic field is passed through a 100 nm silver spectral filter and a 0.5 mrad radius far-field spatial filter to eliminate the long trajectories, producing a spatially uniform temporal profile. Temporal gating of the emission to a single half-cycle is achieved by the short pulse duration,
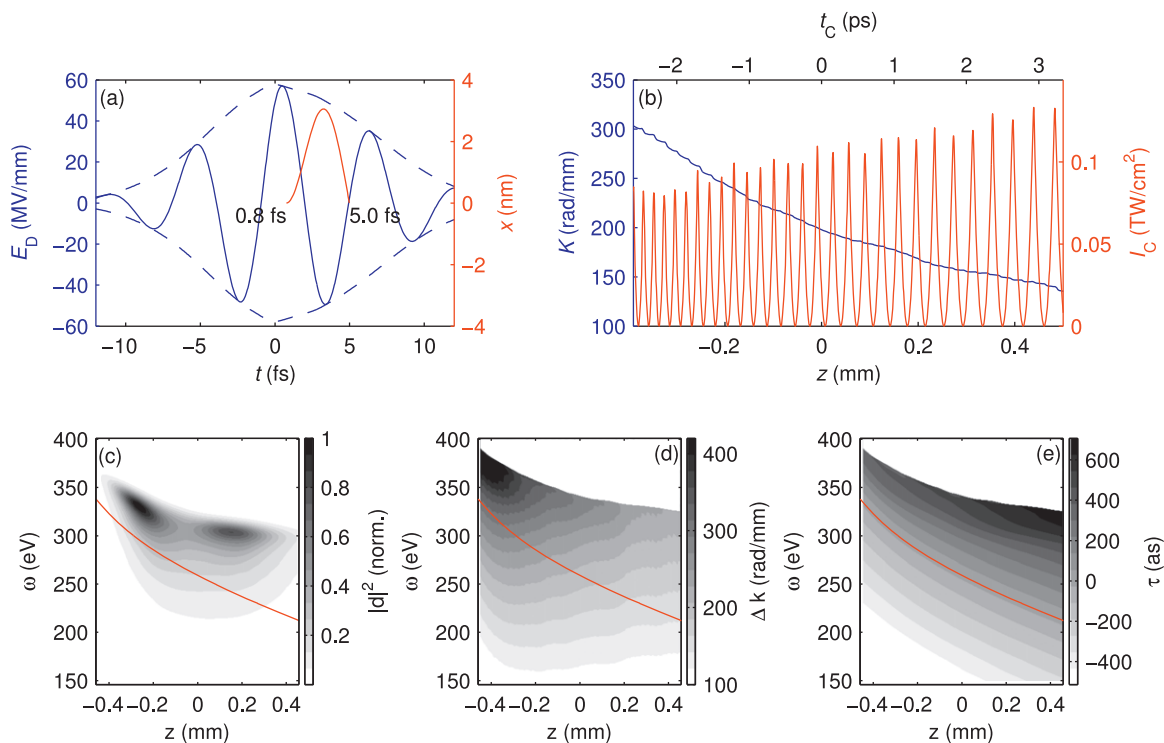
Figure 4. (a) Blue, left y-axis: drive pulse electric field (solid) and envelope (dashed) on axis at the centre of the gas jet ($r = z = 0$). Red, right y-axis: continuum electron trajectory chosen for counterpropagating pulse train (CPT) design with ionization and recombination times indicated. (b) Blue, left y-axis: longitudinal wavenumber of CPT. Red, right y-axis: temporal intensity of CPT. The upper and lower x-axes show time in the counterpropagating frame t_C and longituindal position z respectively. (c)–(e) Properties of the local contribution to the macroscopic field caused by the chosen trajectory, showing intensity (c), phase mismatch (d) and group delay (e). The red line shows the contour of constant group delay chosen for phase matching.

following Goulielmakis *et al* [3]. However, because of the spectral selectivity of the quasi-phase matching, a high-pass spectral filter is not needed.

The retardation of the drive pulse by the neutral helium atoms causes a significant phase mismatch. To design a CPT to correct the phase mismatch and produce a transform limited attosecond pulse, we follow the formalism of sections 2.2 and 2.4. First, we choose the short quantum trajectory in which electrons are born just after the strongest field peak of the pulse as a target for which to design the CPT [3]. This is shown in figure 4(a). Then, we perform an auxillary simulation without a CPT and restricting the range of electron birth and return times to the chosen trajectory. The amplitude of the local contribution to the macroscopic field, $|d(\omega, z)|$ is shown in figure 4(c). At the centre of the jet, which we take as $z = 0$, the classical cutoff is 311 eV. We choose $\omega_C = 259$ eV, located in the plateau, as the nominal centre frequency of the harmonics. From the simulation, we extract the phase mismatch $\Delta k = \partial_z \phi_d$, shown in figure 4(d) and the group delay $\tau = \partial_\omega \phi_d$, shown in figure 4(e). Starting at ($\omega = \omega_C$, $z = 0$), we trace a contour of τ, shown by the red line in figures 4(c)–(e). We extract $K = \Delta k$ along this contour, which is shown in blue in figure 4(b). We choose a centre wavelength of 800 nm for the CPT and evaluate the coefficient α using (13). Finally, (19) gives the temporal intensity
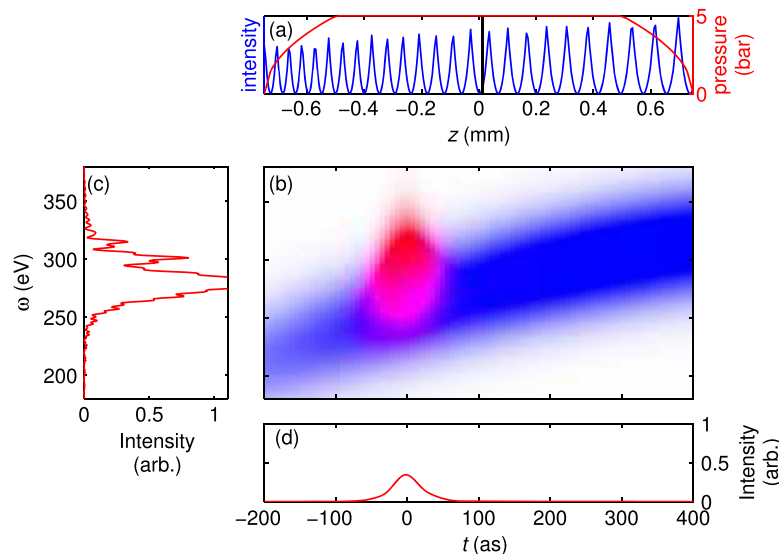
Figure 5. A frame of movie 1, showing dynamics of the transform-limited attosecond pulse production using a chirped counterpropagating pulse train. (a) z position of the drive laser pulse (vertical black line), intensity of the CPT (blue line, left y-axis) and the gas pressure (red, right y-axis). (b) Gabor spectrogram of the local macroscopic contribution from the current z position (blue) and the macroscopic field accumulated up to this point (red). (c) Spectrum and (d) temporal intensity of the accumulated macroscopic field.

envelope of the CPT $I_C(t)$, shown in red in figure 4(b). The spatial profile is taken as a Gaussian beam with waist e^{-2} radius of 50 μm located in the middle of the gas jet. Its total energy is 15 μJ.

With the CPT designed, we can include it in a complete simulation with the full range of birth and recombination times. The dynamics of the generation are illustrated in movie 1 (available at stacks.iop.org/njp/16/113011/mmedia), a frame of which is shown in figure 5. Panel (a) represents the progress of the drive pulse (vertical black line, moving left to right) and the CPT (blue, moving right to left) through the interaction region (local gas pressure shown in red). Panel (c) shows the superposition of two Gabor spectrograms. The blue spectrogram shows the local contribution to the full macroscopic response, including absorption of the harmonics, the far-field spatial filter, and the spectral filter. It is inhibited when the drive pulse overlaps with a peak of the CPT, and therefore appears to flicker with decreasing frequency. Its left to right motion represents delay in the comoving frame, caused by the refractive index of the gas. The red spectrogram shows the macroscopic response accumulated up to the current point in the interaction region. New components are produced in order of decreasing frequency, as determined by the varying quasi-phase matching condition.

The resulting temporal profile is shown in figure 6(a). A 31 as pulse is produced, quite close to the transform limited duration of 20 as. Note that all the temporal and spectral profiles in this paper are radially integrated to infinity (corresponding to the experimental observable in e.g. photoelectron spectroscopy), proving the absence of significant spatio-temporal distortion. To verify that an isolated pulse is produced, figure 6(b) shows a zoomed out temporal profile on a logarithmic scale. Satellite pulses are at the 1% intensity level, below the detection threshold of current experiments [46, 47], and the main pulse contains >90% of the energy. The spectral density and phase, the latter being an intensity-weighted radial average, are shown in
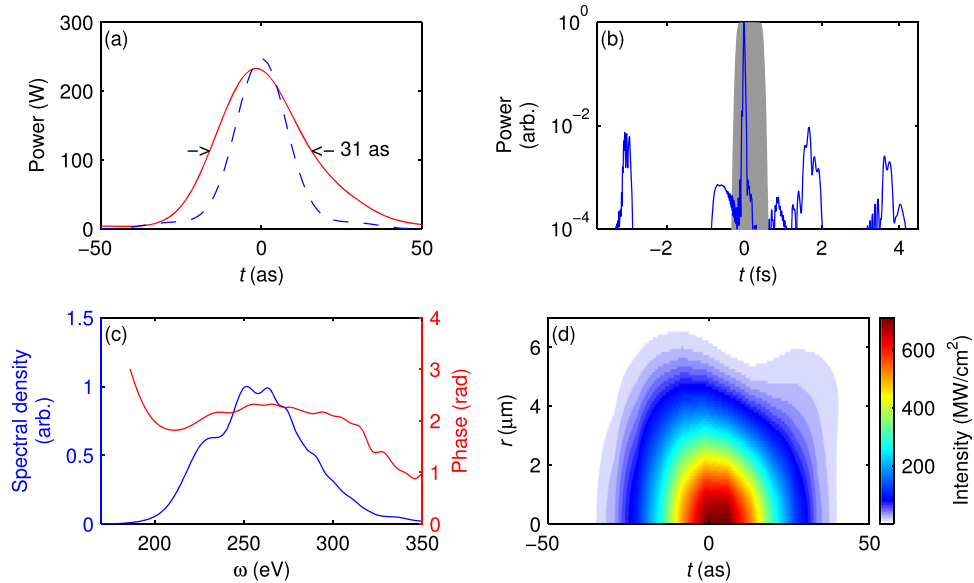
Figure 6. Transform-limited isolated attosecond pulse produced using chirped quasi-phase matching. (a) Instantaneous power of the generated pulse (red solid), with indicated FWHM duration and Fourier-transform limited pulse (blue dashed). (b) Same as (a) but zoomed out and on logarithmic scale. The temporal window used for the spectrum is shown in gray. (c) Spectral density (blue, left y-axis) and phase (red, y-axis). (d) Spatio-temporal intensity at the focus after far-field spatial filtering.

figure 6(c). A maximum phase deviation of 0.6 rad across the full width at 10% bandwidth 204–310 eV shows that the attochirp has been well compensated. In figure 6(c), as with the other spectra in this paper, a numerical window, shown in gray in figure 6(b), has been applied to the temporal profile to prevent the weak satellite pulses from causing fine interference fringes in the spectrum. Finally, figure 6(d) shows spatio-temporal profile that would result if the pulse were refocused without magnification after the far-field spatial filter. The distribution is quite uniform.

Synthesis of the CPT is within the reach of current femtosecond pulse shaping technology. If the CPT were produced by shaping a transform limited pulse, then the required optical bandwidth would be 16 THz (34 nm at 800 nm) and the duration 10 ps, giving a time-bandwidth product of 160, within the capability of a 4f shaper with a spatial-light modulator [7]. More advanced methods, such as the two-dimensional virtually imaged phase array [48], can achieve time-band products of 1000–2000. Furthermore, if the initial pulse is pre-chirped to the full 10 ps duration of the train (using e.g. a block of heavy glass), then only spectral amplitude shaping is required, since the shaped spectrum is mapped into the time domain through the chirp. Since, as shown by figure 3 and equation (21), the harmonic modulation efficiency of the CPT depends only weakly on its optical frequency, a chirped CPT would have a minor effect which could in principle be corrected for. Finally, direct space-to-time shaping [49] may be suitable, since the instantaneous optical phase of the CPT does not matter.
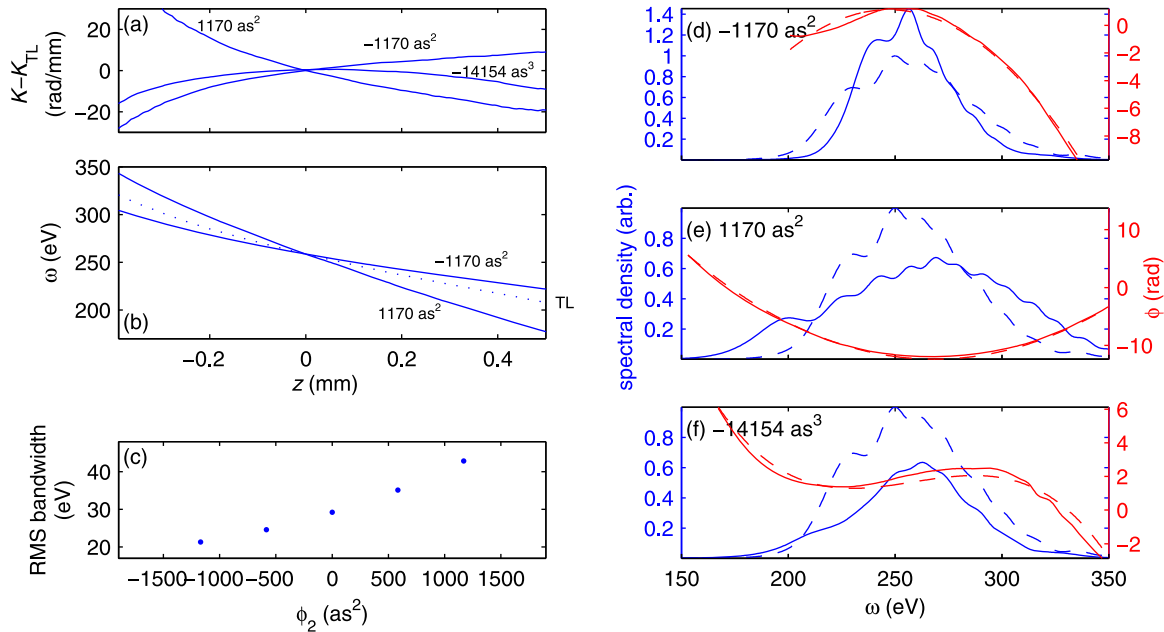
Figure 7. (a) QPM spatial frequency relative to transform-limited case for generation of attosecond pulses with the labelled quadratic (± 1170 as^2) and cubic ($-14\,154$ as^3) spectral phases. (b) Phase-matched harmonic frequency for generation of the labelled quadratic spectral phases and the transform limited case (dashed). (c) Root-mean square bandwidth of the generated pulse versus generated quadratic spectral phase coefficient. (d)–(f) Spectral density (blue, left y-axis) and phase (red, right y-axis) of the resulting attosecond pulses corresponding to (a). The spectral density for the transform-limited case is shown for reference by the dashed blue lines. The spectral phases are blanked out at the 1% intensity level. The target spectral phases are shown by dashed red lines.

3.2. Production of arbitrarily chirped isolated attosecond pulses

We now illustrate the generation of attosecond pulses with a specified group delay curve $\tau_E(\omega)$. The parameters and procedure are identical to the previous section, except that the contour $\omega_P(z)$ is traced along $\tau(\omega, z) - \tau_E(\omega)$. We give three examples: a quadratic spectral phase of of ± 1170 as^2 (± 2 atomic units) and a cubic spectral phase of -14154 as^3 (-1 atomic unit). Figure 7(a) shows the CPT spatial frequencies, relative to the transform limited case K_{TL}, required to produce a quadratic spectral phase. Qualitatively, the curves correspond to the imparted group delay: linear around $z = 0$ for the quadratic spectral phase, and quadratic for the cubic spectral phase. The phases of the resulting attosecond pulses and target phases are shown in figures 7(d)–(f). There is excellent agreement between the actual and target spectral phases. However, the bandwidth of the chirped pulses is different from the transform limited case, shown by the dashed blue lines. This coupling of chirp to bandwidth is caused by clipping of the z-dependent phase matched frequency and is inherent to the method. Figure 7(b) compares the phase-matched frequency versus z of the chirped and transform limited cases. For a positively chirped pulse, closer to the intrinsic attosecond chirp of the dipole response, the phase-matched frequency sweep is faster, and a larger bandwidth is generated within the interaction region. The opposite applies for a negatively chirped pulse. The trend is illustrated in figure 7(c), which shows the root-mean square bandwidth versus the quadratic spectral phase of the generated pulse. In general, the interaction length cannot be arbitrarily increased; plasma-
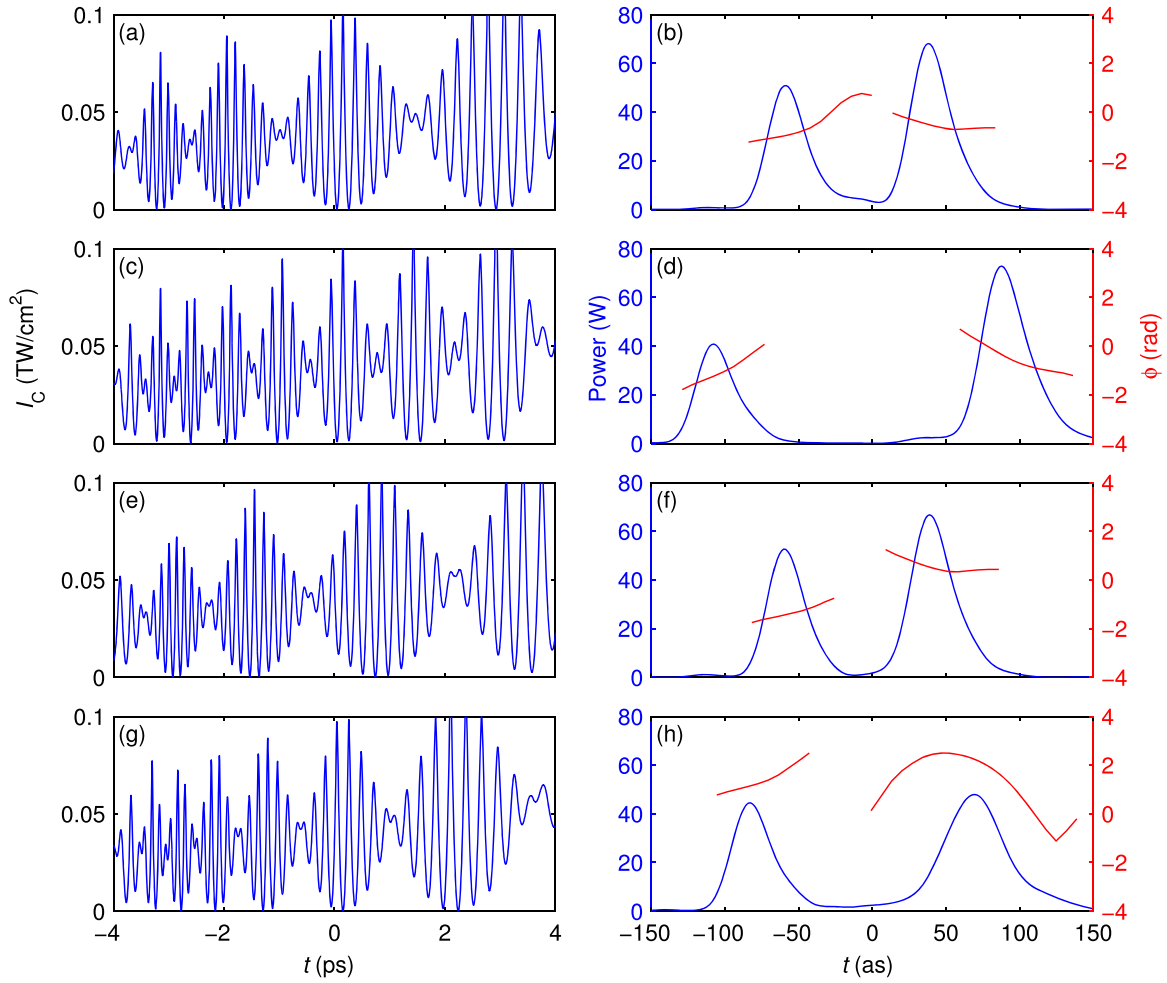
Figure 8. Counterpropagating pulse trains (left column) for the generation of various double attosecond pulses (right column). (a), (b) 97 as separation. (c), (d) 194 as separation. (e), (f) 97 as separation with $\pi/2$ phase shift on the second pulse. (g), (h) 146 as separation with 585 as^2 quadratic spectral phase on the second pulse.

induced defocusing reduces the intensity of the fundamental and the neutral gas absorbs harmonics generated at the start. This sets the ultimate limit to the pulse shaping capability of the method.

3.3. Production of a shaped isolated attosecond pulse

We now illustrate spectral amplitude and phase control over the attosecond pulses using (22). The target filter transfer function is

$$H(\omega) = \frac{e^{i\omega T/2} + e^{-i\omega T/2 + i\phi_0}}{2}, \tag{23}$$

which produces a double pulse with separation T and relative phase ϕ_0. Note that both the amplitude and phase of this filter vary with frequency. Figure 8 shows some results, with CPT profiles in the left column and the resulting pulse sequences in the right column. Panels (a) and
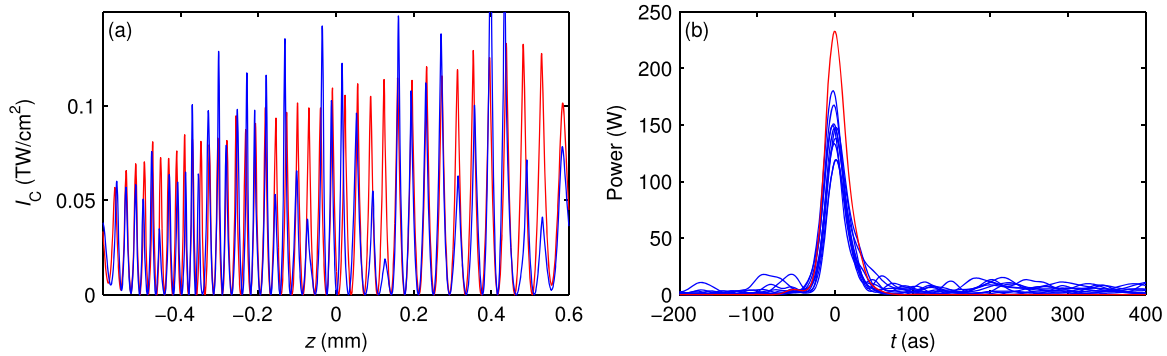
Figure 9. (a) Ideal counterpropagating pulse train for transform limited pulse generation, identical to figure 4 (red), and the same with 20% random error on the peak heights and one eighth of a period peak position error. (b) Attosecond pulses resulting from ideal counterpropagating pulse train (red) and from ten imperfect trains (blue).

(b) have $T = 97$ as and $\phi_0 = 0$. The delay is increased to $T = 197$ as in panels (c) and (d), showing that the delay can be adjusted. Panels (e) and (f) show a relative phase of $\pi/2$ applied to the $T = 97$ as case. Such a capability may be useful for wavepacket interferometry. Finally, panels (g) and (h) show a separation of $T = 146$ as with a 585 as^2 (1 atomic unit) applied to the second pulse only, showing that the phases of the two pulses may be adjusted independently. For further insight into the generation process, movie 2 illustrates the generation of the 97 as separated double pulse using the same format as movie 1 (figure 5).

3.4. Impact of an imperfect CPT

Since its synthesis may be experimentally challenging, we evaluated the impact of an imperfect CPT by adding a random error to the height (standard deviation 20%) and position (standard deviation 1/8 of the mean spacing) of the sub-pulses of the CPT in section 3.1 (the transform limited case). An example of an imperfect CPT is shown in blue in figure 9(a), along with the ideal CPT in red. We performed a set of ten simulations with these non-ideal CPTs to build up an ensemble of the resulting attosecond pulses. Figure 9(b) shows their temporal profiles (blue), along with that of the ideal case (red). The peak height is typically reduced by 40% and there are satellite pulses at the 10% level, but otherwise the attosecond pulses are not significantly degraded. This shows that the method is not excessively impacted by significant imprecision in the CPT.

3.5. Application to many-cycle drive pulses

The proposed method is also applicable to the attosecond pulse trains produced by many-cycle drive pulses, with the caveat that because the individual pulses of the train are produced by laser half cycles with different intensities, their chirp and bandwidth differ, and it is impossible to perfectly compensate all their phases simultaneously. This restriction applies to any method for compensation of the attosecond chirp. (Previous experiments on pulse trains [50], using e.g. RABBIT for phase measurement, only access and control the average phase of each harmonic.) Figure 10 shows the simulated temporal intensity of an attosecond pulse train. The duration of
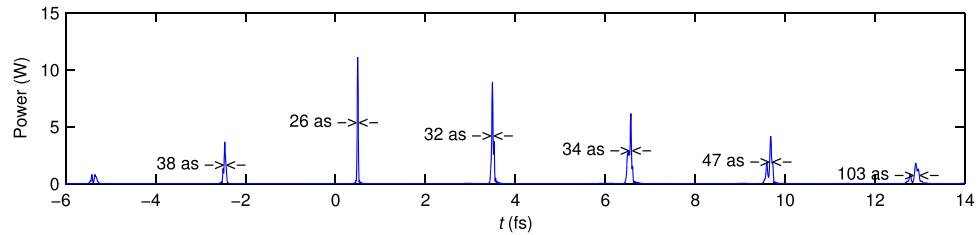
Figure 10. On-axis temporal intensity of the transform-limited attosecond pulse train produced by 30 fs, 550 μJ drive pulse with a chirped counterpropagating pulse train. The FWHM durations of the individual pulses in the train are shown.

the drive pulse is 30 fs and its energy is 550 μJ. All other parameters are equal to those given in section 3.1. The peak intensity of the drive field is reduced compared to the few-cycle case to avoid additional ionization built up during the longer pulse, which causes defocusing [51]. The CPT has been chosen to compress the attosecond burst near $t = 0$, with the result that it is nearly transform limited at the atomic unit of time. The other attosecond bursts are longer, but are significantly compressed compared to the chirped bursts from the single-atom response which are typically hundreds of attoseconds [52].

4. Conclusion

In summary, we have shown that quasi-phase matching HHG with a shaped CPT enables control over the spectral amplitude and phase of an attosecond burst, including elimination of the attosecond chirp. The concept may be applied to any implementation of partial phase matching that permits longitudinal addressing of the modulation frequency, including grating-assisted phase matching [23] which has the potential for high efficiency extension to keV photon energies.

Acknowledgements

References

[1] Nisoli M and Sansone G 2009 *Prog. Quantum Electron.* **33** 17
[2] Krausz F and Ivanov M 2009 *Rev. Mod. Phys.* **81** 163
[3] Goulielmakis E *et al* 2008 *Science* **320** 1614
[4] Hofstetter M *et al* 2011 *Opt. Express* **19** 1767
[5] Ko D H, Kim K T, Park J, Lee J and Nam C H 2010 *New J. Phys.* **12** 063008
[6] Walmsley I, Waxer L and Dorrer C 2001 *Rev. Sci. Instrum.* **72** 1
[7] Weiner A M 2000 *Rev. Sci. Instrum.* **71** 1929

[8] Popmintchev T *et al* 2012 *Science* **336** 1287

[9] Schultze M 2010 *Science* **328** 1658

[10] Cavalieri A L 2007 *Nature* **449** 1029

[11] Remetter T 2006 *Nat. Phys.* **2** 323

[12] Hu S X and Collins L A 2006 *Phys. Rev. Lett.* **96** 073004

[13] Pfeifer T, Spitzenpfeil R, Walter D, Winterfeldt C, Dimler F, Gerber G and Spielmann C 2007 *Opt. Express* **15** 3409

[14] Gaarde M B, Tate J L and Schafer K J 2008 *J. Phys. B: At. Mol. Opt. Phys.* **41** 132001

[15] O'Keeffe K, Robinson T and Hooker S M 2012 *Opt. Express* **20** 6236

[16] Zhang X, Lytle A L, Popmintchev T, Zhou X, Kapteyn H C, Murnane M M and Cohen O 2007 *Nat. Phys.* **3** 270

[17] Paul A, Bartels R A, Tobey R, Green H, Weiman S, Christov I P, Murnane M M, Kapteyn H C and Backus S 2003 *Nature* **421** 51

[18] Gibson E A *et al* 2003 *Science* **302** 95

[19] Dromey B, Zepf M, Landreman M and Hooker S M 2007 *Opt. Express* **15** 7894

[20] Shkolnikov P L, Lago A and Kaplan A E 1994 *Phys. Rev.* A **50** R4461

[21] Peatross J, Voronov S and Prokopovich I 1997 *Opt. Express* **1** 114

[22] Voronov S L, Kohl I, Madsen J B, Simmons J, Terry N, Titensor J, Wang Q and Peatross J 2001 *Phys. Rev. Lett.* **87** 133902

[23] Cohen O, Zhang X, Lytle A L, Popmintchev T, Murnane M M and Kapteyn H C 2007 *Phys. Rev. Lett.* **99** 053902

[24] Salières P *et al* 2001 *Science* **292** 902

[25] Raz O, Pedatzur O, Bruner D B and Dudovich N 2012 *Nat. Photonics* **6** 170

[26] Berry M and Upstill C 1980 *Catastrophe Optics: Morphologies of Caustics and their Diffraction Patterns* (Amsterdam: Elsevier)

[27] Husakou A V and Herrmann J 2001 *Phys. Rev. Lett.* **87** 203901

[28] Couairon A, Brambilla E, Corti T, Majus D, Ramírez-Góngora O and Kolesik M 2011 *Eur. Phys. J. Spec. Top.* **199** 5

[29] Geissler M, Tempea G, Scrinzi A, Schnürer M, Krausz F and Brabec T 1999 *Phys. Rev. Lett.* **83** 2930

[30] Ammosov M, Delone N and Krainov V 1986 *Sov. Phys. JETP* **64** 1191

[31] Tremblay J C and Carrington T Jr 2004 *J. Chem. Phys.* **121** 11535

[32] Yu L, Huang M, Chen M, Chen W, Huang W and Zhu Z 1998 *Opt. Lett.* **23** 409

[33] Lewenstein M, Balcou P, Ivanov M Y, L'Huillier A and Corkum P B 1994 *Phys. Rev.* A **49** 2117

[34] Austin D R and Biegert J 2012 *Phys. Rev.* A **86** 023813

[35] Ivanov M, Brabec T and Burnett N 1996 *Phys. Rev.A* **54** 742

[36] Gordon A and Kärtner F X 2005 *Phys. Rev. Lett.* **95** 223901

[37] Brabec T and Krausz F 2000 *Rev. Mod. Phys.* **72** 545

[38] Le A T, Lucchese R R, Tonzani S, Morishita T and Lin C D 2009 *Phys. Rev.* A **80** 013401

[39] Dudovich N, Smirnova O, Levesque J, Mairesse Y, Ivanov M Y, Villeneuve D M and Corkum P B 2006 *Nat. Phys.* **2** 781

[40] Dahlström J M, Fordell T, Mansten E, Ruchon T, Swoboda M, Klünder K, Gisselbrecht M, L'Huillier A and Mauritsson J 2009 *Phys. Rev.* A **80** 033836

[41] Cohen O, Lytle A L, Zhang X, Murnane M M and Kapteyn H C 2007 *Opt. Lett.* **32** 2975

[42] Verluise F, Laude V, Cheng Z, Spielmann C and Tournois P 2000 *Opt. Lett.* **25** 575

[43] Schmidt B E *et al* 2010 *Appl. Phys. Lett.* **96** 121109

[44] Li C, Wang D, Song L, Liu J, Liu P, Xu C, Leng Y, Li R and Xu Z 2011 *Opt. Express* **19** 6783

[45] Ishii N, Kaneshima K, Kitano K, Kanai T, Watanabe S and Itatani J 2012 *Opt. Lett.* **37** 4182

[46] Chini M, Wang H, Khan S D, Chen S and Chang Z 2009 *Appl. Phys. Lett.* **94** 161112

[47] Gagnon J, Goulielmakis E and Yakovlev V 2008 *Appl. Phys.* B **92** 25

[48] Supradeepa V R, Huang C B, Leaird D E and Weiner A M 2008 *Opt. Express* **16** 11878
[49] Leaird D and Weiner A 2001 *IEEE J. Quantum Elect.* **37** 494
[50] López-Martens R *et al* 2005 *Phys. Rev. Lett.* **94** 033001
[51] Lai C J and Kärtner F X 2011 *Opt. Express* **19** 22377
[52] Mero M, Frassetto F, Villoresi P, Poletto L and Varjú K 2011 *Opt. Express* **19** 23420